A&A 639, A47 (2020)
https://doi.org/10.1051/0004-6361/202037984

Astronomy & Astrophysics

Orbital and spectral characterization of the benchmark T-type brown dwarf HD 19467B⋆,⋆⋆

A.-L. Maire[1,2,⋆⋆⋆], K. Molaverdikhani[2,⋆⋆⋆⋆], S. Desidera[3], T. Trifonov[2], P. Mollière[2], V. D'Orazi[3], N. Frankel[2], J.-L. Baudino[4,5], S. Messina[6], A. Müller[2], B. Charnay[5], A. C. Cheetham[2], P. Delorme[7], R. Ligi[8], M. Bonnefoy[7], W. Brandner[2], D. Mesa[3], F. Cantalloube[2], R. Galicher[5], T. Henning[2], B. A. Biller[9,2], J. Hagelberg[10,7], A.-M. Lagrange[7], B. Lavie[10], E. Rickman[10], D. Ségransan[10], S. Udry[10], G. Chauvin[7,11], R. Gratton[3], M. Langlois[12,13], A. Vigan[13], M. R. Meyer[14], J.-L. Beuzit[13], T. Bhowmik[5], A. Boccaletti[5], C. Lazzoni[3,15], C. Perrot[16,17,5], T. Schmidt[18,5], A. Zurlo[19,20,13], L. Gluck[7], J. Pragt[21], J. Ramos[2], R. Roelfsema[21], A. Roux[7], and J.-F. Sauvage[22,14]

(Affiliations can be found after the references)

Received 19 March 2020 / Accepted 16 May 2020

ABSTRACT

Context. Detecting and characterizing substellar companions for which the luminosity, mass, and age can be determined independently is of utter importance to test and calibrate the evolutionary models due to uncertainties in their formation mechanisms. HD 19467 is a bright and nearby star hosting a cool brown dwarf companion detected with radial velocities and imaging, making it a valuable object for such studies.

Aims. We aim to further characterize the orbital, spectral, and physical properties of the HD 19467 system.

Methods. We present new high-contrast imaging data with the SPHERE and NaCo instruments. We also analyze archival data from the instruments HARPS, NaCo, HIRES, UVES, and ASAS. Furthermore, we use proper motion data of the star from HIPPARCOS and *Gaia*.

Results. We refined the properties of the host star and derived an age of $8.0^{+2.0}_{-1.0}$ Gyr based on isochrones, gyrochronology, and chemical and kinematic arguments. This age estimate is slightly younger than previous age estimates of ∼9–11 Gyr based on isochrones. No orbital curvature is seen in the current imaging, radial velocity, and astrometric data. From a joint fit of the data, we refined the orbital parameters for HD 19467B, including: a period of 398^{+95}_{-93} yr, an inclination of $129.8^{+8.1}_{-5.1}$ deg, an eccentricity of 0.56 ± 0.09, a longitude of the ascending node of 134.8 ± 4.5 deg, and an argument of the periastron of $64.2^{+5.5}_{-6.3}$ deg. We assess a dynamical mass of 74^{+12}_{-9} M_J. The fit with atmospheric models of the spectrophotometric data of the companion indicates an atmosphere without clouds or with very thin clouds, an effective temperature of 1042^{+77}_{-71} K, and a high surface gravity of $5.34^{+0.08}_{-0.09}$ dex. The comparison to model predictions of the bolometric luminosity and dynamical mass of HD 19467B, assuming our system age estimate, indicates a better agreement with the Burrows et al. (1997, ApJ, 491, 856) models; whereas, the other evolutionary models used tend to underestimate its cooling rate.

Key words. brown dwarfs – methods: data analysis – stars: individual: HD 19467 – techniques: high angular resolution – planets and satellites: dynamical evolution and stability – techniques: image processing

1. Introduction

The mass of most substellar companions found around stars with high-contrast imaging techniques is inferred from the comparison of their measured luminosity and estimated age to evolutionary models (e.g., Burrows et al. 1997; Baraffe et al. 2003, 2015; Marley et al. 2007). However, uncertainties in the age estimates and in the initial conditions during the formation of these objects produce large uncertainties in the mass estimates, especially at the boundary of the planet and brown dwarf regimes. To test and calibrate the evolutionary models, the detection and the characterization of benchmark low-mass companions, for which the luminosity, mass, and age can be derived from independent methods, is of paramount importance.

HD 19467 is a G3 main-sequence star located at 32.03 ± 0.11 pc[1] (Gaia Collaboration 2016, 2018). Crepp et al. (2014) infer an age of 4.6–10 Gyr from isochrones and gyrochronology, and a subsolar metallicity of [Fe/H] = −0.15 ± 0.04 dex. Mason et al. (2001) did not find evidence for stellar binarity from speckle interferometry. Crepp et al. (2014) report the discovery of a cool brown dwarf companion from a radial velocity (RV) trend measured with the Keck High Resolution Echelle Spectrometer (HIRES) and subsequently confirmed with near-infrared (NIR) high-contrast imaging with the Keck Near-InfraRed Camera (NIRC2). HD 19467B has an

⋆ The reduced images shown in Fig. 3 are only available at the CDS via anonymous ftp to cdsarc.u-strasbg.fr (130.79.128.5) or via http://cdsarc.u-strasbg.fr/viz-bin/cat/J/A+A/639/A47

⋆⋆ Based on observations collected at the European Organisation for Astronomical Research in the Southern Hemisphere under ESO programmes 1100.C-0481, 0100.C-0234, 096.C-0602, 072.C-0488, 183.C-0972, 084.D-0965, 188.C-0265, 192.C-0852, and 0100.D-0444.

⋆⋆⋆ F.R.S.-FNRS Postdoctoral Researcher.

⋆⋆⋆⋆ International Max Planck Research School for Astronomy and Cosmic Physics, Heidelberg, Germany.

[1] The uncertainty includes an additional uncertainty of 0.1 mas to account for potential parallax systematics, https://www.cosmos.esa.int/web/gaia/dr2

angular separation to the star of ∼1.65″, corresponding to a projected separation of ∼53 au, a flux ratio with respect to the star $\Delta K_s = 12.57 \pm 0.09$ mag, with blue J–H and J–K_s colors, as well as a minimum dynamical mass of $51.9^{+3.6}_{-4.3}$ M_J inferred from the RV acceleration and the projected separation (assuming a distance of 30.86 ± 0.60 pc from HIPPARCOS, van Leeuwen 2007). It is part of a growing group of imaged brown dwarfs of spectral type T with an RV signature, which includes, GJ 758B (Thalmann et al. 2009; Bowler et al. 2018), HD 4113C (Cheetham et al. 2018), GJ 229B (Nakajima et al. 1995; Brandt et al. 2019a), and HD 13724B (Rickman et al. 2020). Such objects are valuable benchmarks for atmospheric and evolutionary models of cool substellar objects.

Subsequent observations of HD 19467B with the integral field spectrometer (IFS) Project 1640 (P1640) include a low-resolution NIR spectrum ($R = 30$), covering the J and H bands, and indicate a spectral type of T5.5 ± 1.0 (Crepp et al. 2015). By fitting the IFS spectrum with BT-Settl models (Allard et al. 2012) with solar metallicity, Crepp et al. (2015) also estimated an effective temperature of $T_{\rm eff} = 978^{+20}_{-43}$ K. Nevertheless, they deemed their surface gravity constraints ($\log g = 4.21$–5.31 dex) to be unreliable by fitting spectra of template T dwarfs, which were degraded and trimmed, to the P1640 resolution and bandwidth. More recently, Jensen-Clem et al. (2016) report a nondetection of the companion in polarized light in the H band using Gemini Planet Imager (GPI) data. The authors assess a degree of linear polarization below 2.4% at 99.73% confidence. This result does not bring any further constraints on the atmospheric properties, in particular, the cloud structure because the expectations for such an object are below 1%. Wood et al. (2019) report a stellar radius measurement of 1.295 ± 0.048 $R_\odot$ using the Center for High Angular Resolution Astronomy (CHARA) interferometer. The authors also find an isochronal age of the system of $10.06^{+1.16}_{-0.82}$ Gyr and that evolutionary models underpredict the bolometric luminosity of the companion ($-5.19^{+0.06}_{-0.07}$ dex) by ∼0.5 dex, assuming the isochronal age of the system and the minimum dynamical mass derived in Crepp et al. (2014). Recently, Bowler et al. (2020) present an orbital analysis of the companion using new and archival Keck/NIRC2 imaging data spanning ∼6.5 yr. They derived (median values and 68.3% credible intervals) a semi-major axis of 56^{+15}_{-25} au, an eccentricity of $0.39^{+0.26}_{-0.18}$, an inclination of $125.0^{+9.4}_{-14.0}$ deg, a longitude of the node of 113^{+16}_{-41} deg, and an argument of the periastron of 66^{+32}_{-44} deg (the last two parameters are restricted to the interval [0,180) deg because of ambiguities due to the use of imaging data only). Mesa et al. (2020) present a long slit spectrum at a resolution of ∼350 over the YJH bands, which was obtained with the Spectro-Polarimetric High-contrast Exoplanet REsearch (SPHERE) instrument. They derived a spectral type of T6 ± 1 and an effective temperature of 1000 ± 100 K by fitting BT-Settl spectra, in agreement with Crepp et al. (2015). They also derived a surface gravity of 5.0 ± 0.5 dex, in the high range of the values in Crepp et al. (2015).

We present here NIR follow-up observations of HD 19467B with the SPHERE instrument (Beuzit et al. 2019) at the Very Large Telescope (VLT), taken as part of the SpHere INfrared survey for Exoplanets (SHINE, Chauvin et al. 2017a). We also present complementary observations in the thermal IR with the Nasmyth Adaptive Optics System and Near-Infrared Imager and Spectrograph (NaCo, Rousset et al. 2003; Lenzen et al. 2003). In addition, we analyze archival RV data from the High Accuracy Radial velocity Planet Searcher (HARPS, Mayor et al. 2003) and HIRES (Vogt et al. 1994), archival imaging data from NaCo, archival spectroscopic data from HARPS and the Ultraviolet and Visual Echelle Spectrograph (UVES, Dekker et al. 2000), as well as archival photometric data from the All Sky Automated Survey (ASAS, Pojmanski 1997). Furthermore, we use proper motion measurements of the star from HIPPARCOS and *Gaia*. We present an updated analysis of the properties of the host star in Sect. 2. We describe the new high-contrast imaging observations and the archival RV data that we use to further characterize HD 19467B in Sect. 3. We fit the SPHERE, NIRC2, HARPS, HIRES, and HIPPARCOS-*Gaia* data simultaneously and derive orbital parameters and a dynamical mass for HD 19467B in Sect. 4. Section 5 discusses the spectral properties of the companion using our new photometric data and literature measurements. Finally, we compare the dynamical and spectral properties of HD 19467B to model predictions in Sect. 6.

2. Properties of the host star

Crepp et al. (2014) note that HD 19467 is a field star not associated to any moving group. They also find that given that it is located slightly above the median HIPPARCOS-based main sequence (Wright 2005) and has subsolar metallicity, it should be older than the Sun (4.6 Gyr).

Considering the relevance of the stellar age for the goals of our study, we present here a comprehensive reassesment of the age of the system and other stellar properties. Our approach is based on the inclusion of a variety of indicators, as in Desidera et al. (2015).

2.1. Abundance analysis

We retrieved and analyzed archival data from HARPS and UVES to perform a spectroscopic determination of stellar parameters ($T_{\rm eff}$, $\log g$, and microturbulence velocity ξ) and elemental abundances for light, iron-peak, and α elements. The signal-to-noise ratio on the HARPS spectrum is ∼400. The analysis of the HARPS spectrum was carried out in the standard way, as described in our previous work (see, e.g., D'Orazi et al. 2017), by using the Kurucz set of model atmospheres (Castelli & Kurucz 2003) and the code MOOG by Sneden (1973, 2017 version). Briefly, effective temperature and microturbulence come from removing spurious trends between iron abundances from FeI lines and excitation potential and reduced equivalent width of the spectral lines, respectively. Surface gravity has been obtained via ionization equilibrium of FeI and FeII. We refer the reader to D'Orazi et al. (2017) for details on linelist, atomic parameters and error estimate computations.

We derived $T_{\rm eff} = 5770 \pm 80$ K, $\log g = 4.32 \pm 0.06$ dex, and a microturbulent velocity $\xi = 1.00 \pm 0.15$ km s^{-1}. The $T_{\rm eff}$ is slightly higher and the $\log g$ is slightly lower than those derived in Crepp et al. (2014): $T_{\rm eff} = 5680 \pm 40$ K and $\log g = 4.40 \pm 0.06$ dex. We also derived [Fe/H] = −0.11 ± 0.01 dex, [C/H] = −0.09 ± 0.01 dex, [O/H] = −0.02 ± 0.01 dex (non local thermal equilibrium corrections applied), [Na/H] = −0.03 ± 0.01 dex, [Mg/H] = 0.05 ± 0.08 dex, [Al/H] = 0.05 ± 0.03 dex, [Si/H] = −0.04 ± 0.04 dex, [S/H] = −0.09 ± 0.07 dex, [Ca/H] = −0.04 ± 0.05 dex, [Ti/H]I = 0.03 ± 0.05 dex, [Ti/H]II = 0.09 ± 0.02 dex, [Cr/H]I = −0.09 ± 0.03 dex, [Cr/H]II = −0.07 ± 0.06 dex, and [Ni/H] = −0.09 ± 0.05 dex. The [α/Fe] ratios are very weakly enhanced (at the level of ∼0.1 dex). This abundance pattern is not compatible with a thick disk membership and suggests membership to the thin disk population or to the small population intermediate between the thin disk and the thick disk proposed by Fuhrmann & Chini (2019) and references therein.

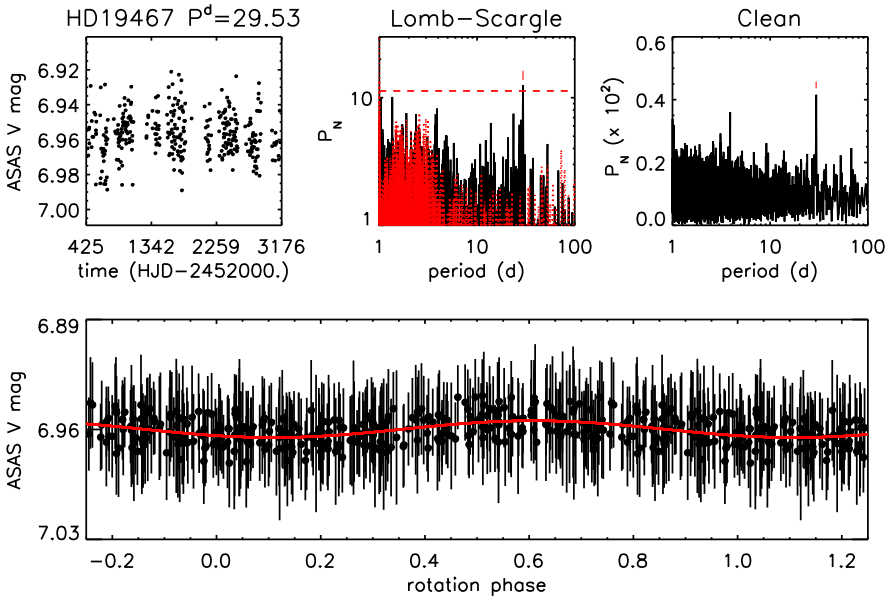

Fig. 1. Photometric analysis of HD 19467 based on ASAS data. *Top row from left to right*: V-band magnitude vs. Heliocentric Julian Day, Lomb-Scargle periodogram, and *CLEAN* periodogram. For the Lomb-Scargle periodogram, we show the spectral window function (in red), the 99% confidence level (horizontal dashed red line), and the peak corresponding to the rotation period (red vertical mark). *Bottom panel*: light curve phased with the rotation period. The solid red curve represents the sinusoidal fit.

The UVES spectrum was used to derive the oxygen abundance from the 7700 Å triplet. The C/O ratio in number is 0.52, which is similar to the value for the Sun (~0.54, Asplund et al. 2009; Caffau et al. 2011). This also argues against a thick disk membership.

Abundance ratios involving neutron capture elements can be used as age indicators. From the measured [Y/Mg] = −0.15 ± 0.07 dex, we infer an age of 8.5 Gyr following Nissen (2016) and 7.7 Gyr using Spina et al. (2018).

2.2. Isochrone fitting

As mentioned above, the star is slightly evolved above the main sequence, making it suitable for age determination using isochrones. Crepp et al. (2014) estimated an age of 9 ± 1 Gyr, while Wood et al. (2019) derived $10.06^{+1.16}_{-0.82}$ Gyr exploiting also the interferometric measurement of the stellar radius. We obtained an independent determination using the models by Bressan et al. (2012) exploiting the online tool for Bayesian determination of stellar parameters PARAM[2] (da Silva et al. 2006). Using as input our spectroscopic effective temperature and metallicity, the V band magnitude from HIPPARCOS (7.00 mag) and the *Gaia* DR2 parallax, we obtain a stellar age of 9.3 ± 1.6 Gyr and a stellar mass of 0.953 ± 0.022 $M_\odot$. All these estimates then converge on a very old age for the system. The RV time series and the adaptive optics observations presented here allow us to rule out that the position in the color-magnitude diagram is altered by binarity, the contribution of HD 19467B to the integrated flux being negligible.

2.3. Photometric analysis

To better constrain the stellar rotation period and age through gyrochronology, we analyzed photometric data from ASAS using the approach in Messina et al. (2010). Figure 1 shows the results. Both the Lomb-Scargle periodogram (Lomb 1976; Scargle 1982) and the *CLEAN* periodogram (Roberts et al. 1987) show a peak at $P_\star = 29.53 \pm 0.16$ d. The uncertainty was estimated following the approach of Lamm et al. (2004). Our rotation period estimate is longer by ~1.8σ than the indirect estimate of 24.9±2.5 d in Crepp et al. (2014) based on the measured chromospheric activity indicator $\log R'_{\rm HK}$ and $B-V$ color (Wright et al. 2004). As a result, our gyrochronological age estimate of 5.6 ± 0.8 Gyr points toward older ages than the age estimate of 3.1–5.3 Gyr in Crepp et al. (2014) based on the same model relations in Mamajek & Hillenbrand (2008). Our older age estimate is consistent with the slow $v \sin i_\star = 1.6 \pm 0.5$ km s^{-1} of the star (Crepp et al. 2014). We also derived an age of 5.8 ± 0.6 Gyr using the gyrochronological calibration in Delorme et al. (2011). The uncertainty is dominated by the calibration errors calculated from the dispersion of periods around the Hyades and Praesepe calibration sample.

Combining the rotation period, the stellar radius (1.295 ± 0.048 $R_\odot$, Wood et al. 2019), and the projected rotational velocity, we infer using a Monte Carlo approach and Gaussian distributions for the three input parameters an inclination of the stellar rotation axis with respect to the line of sight of 46^{+20}_{-15} deg or 137^{+18}_{-17} deg with the uncertainties given at 68%. The wide ranges are due to the large uncertainty on the projected rotational velocity. The two sets of values are due to the degeneracy of the sin function (see Eq. (3) in Bonnefoy et al. 2018). As explained in Bowler et al. (2017) and Bonnefoy et al. (2018), a lower limit on the relative orientation of a stellar spin axis and of the orbital angular momentum or true obliquity of a companion can be derived from the absolute difference between the posterior distribution of the orbital inclination of the companion (derived in Sect. 4 for HD 19467B) and of the posterior distribution of the inclination of the rotation axis of the star. For the latter, we only consider the range [90, 180] deg. The resulting distribution extends down to zero. From the upper bound of the 68% interval, we infer that the configuration of the star-brown dwarf system is compatible with a spin-orbit alignment or misalignment within 30° at 68%.

2.4. Milky Way evolution model

We also used a Milky Way evolution model approach (Frankel et al. 2018, 2019) to constrain the stellar age given its present-day distance to the Milky Way center and its slight subsolar metallicity. Such an analysis is applicable for stars with low enhancements in α elements similar to HD 19467. The model

[2] http://stev.oapd.inaf.it/cgi-bin/param_1.3

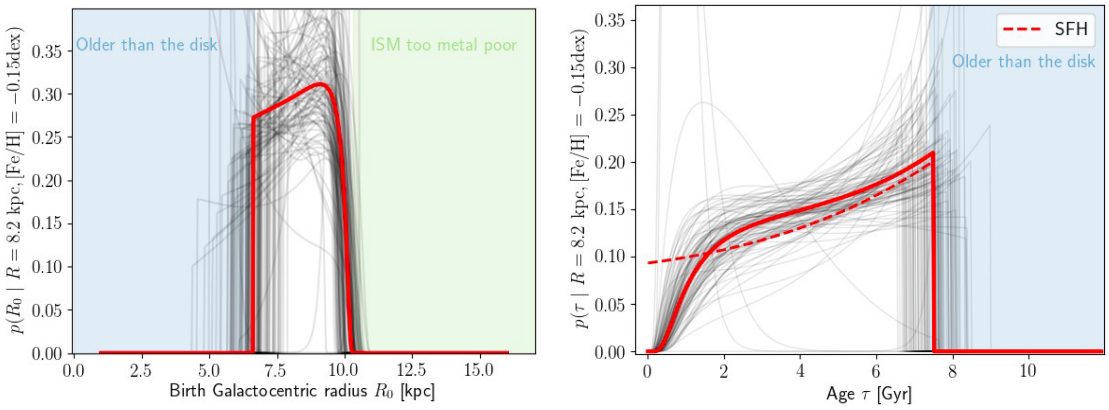

Fig. 2. PDF of the birth Galactocentric radius (*left*) and of the age (*right*) of HD 19467 derived using an evolution model of the Milky Way (see text). In both panels, the red thick curves show the best-fit and the gray curves are drawn using the uncertainties in the model parameters. In the right panel, the red dashed curve represents the age PDF assuming only that HD 19467 belongs to the Milky Way disk.

assumes a radial-dependent star formation history for the Milky Way, a relation for the stellar metallicity at their formation epoch as a function of their distance to the Milky Way center and their formation epoch, and the migration distance from their birth place as a function of time after birth.

The left panel of Fig. 2 shows the probability density function (PDF) of the birth distance of HD 19467 at given present-day distance and metallicity (see red thick curve). The constraints come from two main aspects. First, given that HD 19467 is metal poor, it cannot come from less than 6.8 kpc (or it would need to be older than the Milky Way thin disk). Then, it cannot either come from farther than 10 kpc, because beyond this distance the interstellar medium is metal poorer.

The right panel of Fig. 2 gives the PDF of the age of HD 19467 at given present-day radius and metallicity. The red dashed curve represents the star formation history of the Milky Way disk. It would be the age PDF of HD 19467 if we only assume that the star belongs to the Milky Way disk. If, additionally, information on the stellar metallicity and present-radius distance is available, the age PDF can be slightly narrowed down (see red thick curve) to a smoothed version of the local star formation history. However, because radial migration of stars belonging to the Milky Way disk is significant, the solar neighborhood is populated by a large portion of stars that come from very different birth distances with several star formation and metal enrichment histories. This implies that a Galactic evolution approach cannot put tight constraints on the age of HD 19467. Moreover, the age of the Milky Way disk is not well constrained. This results in large uncertainties in the age PDF of HD 19467 in addition to other uncertainties in the model parameters (shown as gray curves). The most robust information that we can derive from our approach is an estimate of the oldest age of HD 19467. Our analysis suggests a value of 7.5 ± 0.9 Gyr.

2.5. Summary

We summarize here the results of the various methods of determining the stellar age (see also Table 1). Using ASAS photometric data of HD 19467, we derived a direct gyrochronological age of 5.6 ± 0.8 Gyr, which is older than the indirect estimate of 3.1–5.3 Gyr from activity indicators and colors in Crepp et al. (2014). This still disagrees with isochronal age estimates (9.2–11.2 Gyr, Wood et al. 2019) and our isochronal age estimate (7.7–10.9 Gyr). Our abundance analysis from HARPS and UVES spectra indicates a C/O ratio similar to the Sun, which argues against a ~10-Gyr age. Another argument against such an extremely old age comes from the chemical abundances and kinematics of the star, which suggest that it belongs to the thin disk population. Literature studies constrain the age of the oldest members of this population to 8 Gyr (e.g., Fuhrmann et al. 2017). The abundance of neutron capture elements also indicates an age similar to the thin-disk limit, 7.7–8.5 Gyr. The mild enhancement of α elements is also compatible with the intermediate population between the thin disk and the thick disk, while kinematic parameters would be unusual for a member of this population and more typical of a thin disk star. Fuhrmann & Chini (2019) derived an age of about 10 Gyr for this intermediate population, similar to the age derived through the isochrone method.

Table 1. Summary of age estimates for HD 19467.

Method	Age (Gyr)
Isochrones	9.3 ± 1.6
Kinematics	≤ 8
C/O ratio	<10
Y/Mg ratio	7.7–8.5
Gyrochronology	6.5 ± 0.8
Milky Way evolution model	$<7.5 \pm 0.9$
Adopted value	$8.0^{+2.0}_{-1.0}$

Gyrochronology is expected to be reliable for old stars from theory (because they are less affected by the initial conditions), although in practice precise rotation period measurements are more difficult because stellar spots are usually smaller. This induces a larger scatter in the model relations at old ages. However, Amard & Matt (2020) show that metal-poor stars spin down less effectively at ages older than ~1 Gyr, making them appear younger than they are actually. For a star with an [Fe/H] similar to HD 19467 (−0.11 dex) and a rotation period of 29.5 d, the age estimated from gyrochronology would shift from ~5.8 to ~6.5–6.8 Gyr according to the assumed wind-braking model (see Fig. 2 in Amard & Matt 2020). In addition, van Saders et al. (2016) show that Sun-like stars older than 4–5 Gyr can experience weakened magnetic braking, which would also bias gyrochronological age estimates toward younger values. Assuming that the rotational evolution of HD 19467 is not

Table 2. Observing log.

UT date	ϵ ($''$)	τ_0 (ms)	AM start/end	Instrument	Bands	DIT (s) × Nfr	FoV rot. (°)	SR
2015/12/20	0.6–0.9	2–3	1.05–1.04	NaCo	M'	$0.08 \times 45\,000$	90	–
2017/10/06	0.5–0.8	4–6	1.02–1.05	NaCo	L'	$0.10 \times 32\,680$	71.3	–
2017/11/04	0.3–0.9	1–25	1.06–1.02	SPHERE	$K12$	64×66	63.3	0.60–0.87
2018/10/18	0.3–0.6	5–11	1.02–1.04	SPHERE	YJ+$H23$	$64(96) \times 50(33)$	50.2	0.82–0.87

Notes. The columns provide the observing date, the seeing and coherence time measured by the differential image motion monitor (DIMM) at 0.5 μm, the airmass at the beginning and the end of the sequence, the observing mode, the spectral bands, the DIT (detector integration time) multiplied by the number of frames in the sequence, the field of view rotation, and the Strehl ratio measured by the adaptive optics system (at 1.6 μm, SPHERE data only). For the DIT × Nfr column, the numbers in parentheses are for the IFS data.

affected by weakened magnetic braking, our gyrochronological analysis would imply a nominal age of at least ~6.5 Gyr from our measured rotation period.

We then consider the gyrochronological age as a lower limit. The age of the oldest thin disk stars (8 Gyr) is the most probable value for HD 19467. The age of 8 Gyr seems very consistent with large scale surveys of Milky Way disk stars (Pinsonneault et al. 2019). The conflict with the isochrone results can be considered as marginal. We adopt an age of $8.0^{+2.0}_{-1.0}$ Gyr for HD 19467. The lower limit of about 7 Gyr is set by the isochrones and abundance of neutron-capture elements. The upper limit of 10 Gyr corresponds to the case of the star being a member of the intermediate population between the thin disk and the thick disk. Asteroseismological measurements of the star (Ulrich 1986) should provide independent clues on its age and hopefully solve for the discrepancies between gyrochronology and isochrones.

3. Observations and data analysis

3.1. High-contrast imaging

3.1.1. SPHERE NIR observations

HD 19467 was observed twice with SPHERE in the NIR (Table 2). For the 2017 observation, we only used the Infra-Red Dual-band Imager and Spectrograph IRDIS (Dohlen et al. 2008; Vigan et al. 2010) in the dual-band imaging mode with the $K12$ filter pair. For the 2018 observation, we used the standard IRDIFS mode, which allows for simultaneous observations with IRDIS with the $H23$ filter pair and the integral field spectrograph IFS (Claudi et al. 2008) in the YJ bands.

For both sequences, an apodized pupil Lyot coronagraph (Carbillet et al. 2011; Martinez et al. 2009) was used. For calibrating the flux of the images, we acquired unsaturated noncoronagraphic images of the star (hereafter reference point-spread function or reference PSF) at the beginning and end of the sequences. To minimize the frame centering uncertainties in the astrometric error budget, the coronagraphic images were recorded with four artificial crosswise replicas of the star (Langlois et al. 2013). Night-time sky background frames were taken and additional daytime calibration performed following the standard procedure at ESO.

The data were reduced with the SPHERE Data Center pipeline (Delorme et al. 2017a), which uses the Data Reduction and Handling software (v0.15.0, Pavlov et al. 2008) and custom routines. It corrected for the cosmetics and instrument distortion, registered the frames, and normalized their flux. For the IFS data (Mesa et al. 2015), it also calibrated them spectrally and extracted the image cubes. Subsequently, we sorted the frames using visual inspection to reject poor-quality frames (adaptive optics open loops, low-wind effect) and an automatic criterion to reject frames with low flux in the coronagraphic spot (semi-transparent mask). After this step, we were left with 91 and 80% of the frames for the 2017 and 2018 IRDIS data, respectively. We kept all the IFS frames. Finally, the data were analyzed with a consortium image processing pipeline (Galicher et al. 2018) and with the ANgular DiffeRential Optimal Method Exoplanet Detection Algorithm (ANDROMEDA, Mugnier et al. 2009; Cantalloube et al. 2015). Figure 3 shows the images processed with angular differential imaging (ADI, Marois et al. 2006) with the Template Locally Optimized Combination of Images algorithm (TLOCI, Marois et al. 2014) provided in the consortium image processing pipeline.

3.1.2. NaCo thermal IR observations

We also obtained high-contrast imaging data in the L' band with NaCo (Table 2, program ID: 0100.C-0234, PI: Maire). These observations were performed without a coronagraph, in pupil-tracking mode to take advantage of ADI, and in dithering mode to sample the sky background while maximizing the observing efficiency. The data were reduced using a custom reduction pipeline (cosmetics, frame registering, and frame binning by 380, Müller et al. 2018) and analyzed with the TLOCI and ANDROMEDA high-contrast imaging algorithms. Figure 3 shows the image processed with TLOCI and smoothed with a Gaussian with a width of 2 pixels.

Finally, we analyzed archival NaCo data taken with the M' filter (program ID: 096.C-0602, PI: Buenzli). These observations were acquired following the same strategy as for the NaCo/L' data. We processed the data with a custom data reduction and analysis pipeline (Cheetham et al. 2019) by applying a frame binning of 250. Figure 3 shows the processed image smoothed with a Gaussian with a width of 2 pixels. We find no significant signal at the expected location of the companion. We estimated an upper limit for the companion contrast of 9.0 mag based on the 3σ detection limit measured at the expected separation. We verified that fake companions injected into the raw data with this contrast are recovered in the processed image.

3.1.3. Photometry and astrometry

For the high-contrast imaging data where the companion could be recovered, the astrometry and photometry listed in Tables 3 and 4 was measured in the TLOCI images using the fit of a

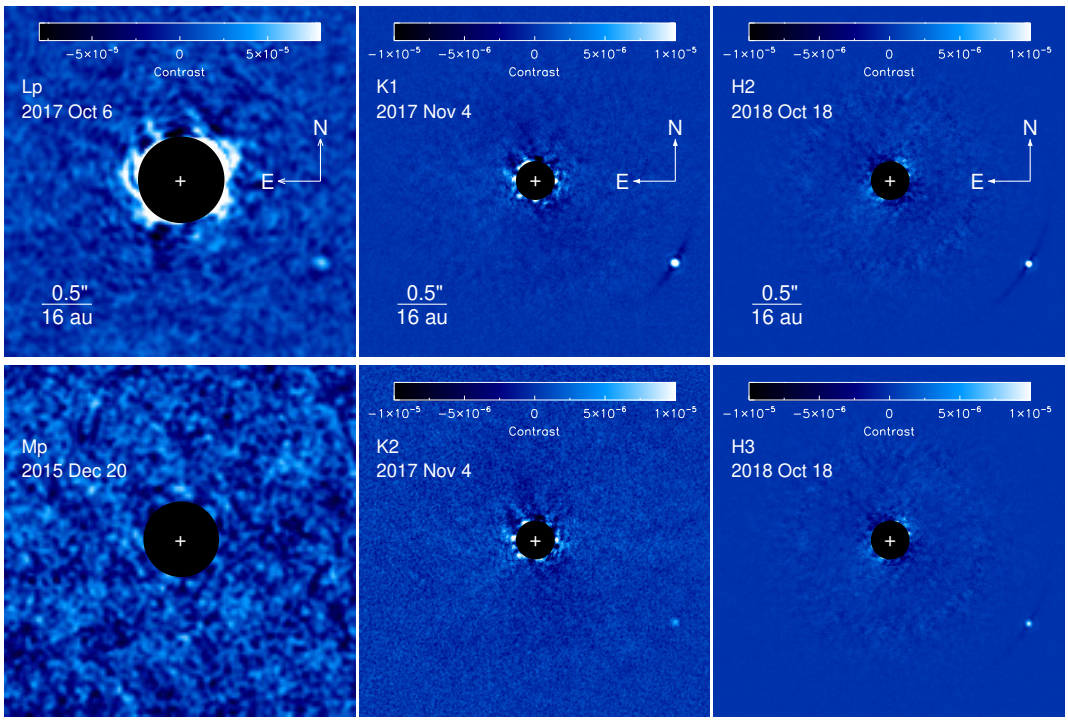

Fig. 3. ADI-processed images of HD 19467 obtained with NaCo (*left panels*) and SPHERE (*other panels*). See text for details. The central regions of the images are numerically masked out to hide bright stellar residuals. The white crosses indicate the location of the star. The brown dwarf companion HD 19467B is seen in the bottom-right part of all images. The poorer quality of the detection in the $K2$ filter is due to strong methane absorption in the atmosphere of the object.

Table 3. Astrometry relative to the star of HD 19467B.

BJD-2 450 000	Filter	ρ (mas)	PA (°)	Pixel scale (mas pix^{-1})	North correction angle (°)
8032.3	L'	1637 ± 19	238.68 ± 0.47	27.20 ± 0.05	-0.5 ± 0.1
8061.2	$K1$	1636.7 ± 1.8	239.39 ± 0.13	12.267 ± 0.009	-1.745 ± 0.053
8061.2	$K2$	1634.4 ± 5.0	239.44 ± 0.21	12.263 ± 0.009	-1.745 ± 0.053
8409.3	$H2$	1631.4 ± 1.6	238.88 ± 0.12	12.255 ± 0.009	-1.804 ± 0.043
8409.3	$H3$	1631.4 ± 1.6	238.88 ± 0.12	12.251 ± 0.009	-1.804 ± 0.043

Notes. The astrometric uncertainties were derived assuming an error budget including the measurement uncertainties (image post-processing) and the systematic uncertainties (calibration).

Table 4. Photometry relative to the star of HD 19467B.

Filter	λ_0 (μm)	$\Delta\lambda$ (μm)	Δmag (mag)	App. mag. (mag)	Abs. mag. (mag)	Flux ($\times 10^{-16}$ W m^{-2} μm^{-1})
$H2$	1.593	0.052	11.50 ± 0.04	16.95 ± 0.05	14.42 ± 0.05	1.953 ± 0.075
$H3$	1.667	0.054	12.43 ± 0.04	17.88 ± 0.05	15.35 ± 0.05	0.734 ± 0.027
$K1$	2.110	0.102	11.52 ± 0.07	16.92 ± 0.07	14.39 ± 0.08	0.750 ± 0.049
$K2$	2.251	0.109	13.12 ± 0.08	18.52 ± 0.08	15.99 ± 0.09	0.133 ± 0.010
L'	3.800	0.620	10.16 ± 0.14	15.46 ± 0.17	12.93 ± 0.17	0.288 ± 0.037
M'	4.780	0.590	>9.0	>14.0	>11.5	<0.332

Notes. The photometric uncertainties were derived assuming an error budget including the measurement uncertainties (image post-processing) and the systematic uncertainties (temporal variability of the reference PSF and of the sequence).

model of the planet image built from the reference PSF and processed with TLOCI (Galicher et al. 2018). The position and flux of the model of the planet image was optimized to minimize the image residuals within a circular region of radius 1.5 full width at half maximum centered on the measured planet location. The astrometry was calibrated following the methods in Maire et al. (2016) for the SPHERE data and in Cheetham et al. (2019) for the NaCo L' data. We compared the TLOCI photometry and

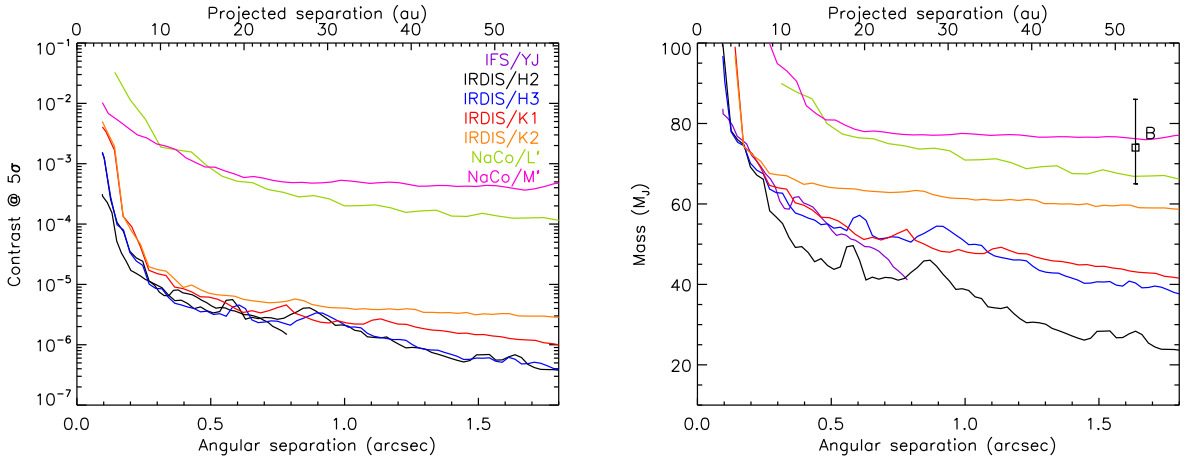

Fig. 4. 5σ detection limits expressed in contrast with respect to the star (*left*) and in companion mass (*right*) for the set of instruments (SPHERE IRDIS and IFS, NaCo) and filters (colored curves). In the *right panel*, we also indicate the location of HD 19467B assuming the mass inferred from the orbital fit (Sect. 4). The mass limits achieved at low masses with the $H3$ and $K2$ filters are degraded compared to those with the $H2$ and $K1$ filters because these filters match methane absorption bands (see also Fig. 3).

astrometry with the ANDROMEDA results and found the values to agree within the TLOCI measurement uncertainties (results not shown). We use the TLOCI measurements for the orbital and spectral analyses in the next sections, because TLOCI has been tested and validated on a larger number of SPHERE datasets to retrieve the astrometry and photometry of detected companions (Galicher et al. 2018). We note that the position angle measured with NaCo is smaller by ~0.7° (~1.4σ) than the position angle measured with SPHERE in a dataset obtained just a month after the NaCo observation.

The absolute magnitudes of the companion at wavelengths shorter than 3 μm were computed assuming for the stellar magnitudes the 2MASS values (Cutri et al. 2003). The absolute magnitudes of the companion at wavelengths longer than 3 μm were computed using stellar magnitudes in the L' band of 5.3 ± 0.1 mag and in the M' band of 5.1 ± 0.1 mag estimated by interpolating the WISE W1 and W2 magnitudes (Cutri & et al. 2013).

3.1.4. Detection limits

The SPHERE and NaCo/L' detection limits were computed using the TLOCI-ADI reductions. The NaCo/M' detection limit was computed using the principal component analysis (PCA) algorithm described in Cheetham et al. (2019) with 54 modes (30% of available modes). The detection limits shown in Fig. 4 account for the small sample statistics correction (Mawet et al. 2014) and, for the SPHERE datasets, for the coronagraph transmissions (Boccaletti et al. 2018). The conversion from contrast to the star into companion mass was computed using a system age of 8 Gyr and "hot-start" atmospheric and evolutionary models of Baraffe et al. (2015, 2003) for the SPHERE data and of Allard et al. (2012) and Baraffe et al. (2003) for the NaCo data. Given the age of the star, we do not expect significant variations in the luminosity-mass relation according to the initial conditions assumed in the evolutionary model (Marley et al. 2007). The SPHERE data provide deeper constraints in contrasts and companion masses. Contrasts as deep as 10^{-5} are achieved beyond 0.3″ (10 au), which exclude additional companions more massive than ~55 M_J. Additional companions more massive than 35 M_J are excluded beyond 1.1″ (35 au).

We also show the mass and angular separation of HD 19467B in the right panel of Fig. 4 assuming the mass derived in Sect. 4. If the companion is more massive than ~77 M_J, it should have been detected in our NaCo M' data.

3.2. Radial velocity data

3.2.1. HIRES

We analyzed the HIRES RV data presented in Butler et al. (2017) following the methods described in Tal-Or et al. (2019), which corrected in particular for small systematics due to an instrument upgrade in August 2004 (BJD epoch 2 453 236). Compared to the data presented in Crepp et al. (2014), the data baseline is increased by ~11 months. The data exhibit a decreasing linear trend (see Appendix B and Sect. 4.3). We fit a linear trend to the data using the Affine-Invariant Markov chain Monte Carlo (MCMC) Ensemble Sampler (Goodman & Weare 2010) provided in the package `emcee` (Foreman-Mackey et al. 2013) to estimate an acceleration of -1.43 ± 0.04 m s^{-1} yr^{-1} (68%). This is included in the uncertainties of the value of -1.37 ± 0.09 m s^{-1} yr^{-1} in Crepp et al. (2014).

3.2.2. HARPS

We also analyzed archival RV data from HARPS taken from 2003 to 2017 (program IDs: 072.C-0488 PI: Mayor, 183.C-0972: PI: Udry, 188.C-0265 PI: Melendez, 192.C-0852 PI: Udry, and 0100.D-0444 PI: Lorenzo de Oliveira). The methods and the data are presented in Trifonov et al. (2020). Some of the HARPS data were taken after an instrument upgrade in June 2015 (Lo Curto et al. 2015, BJD epoch 2 457 177). They display an offset toward larger RVs with the pre-upgrade data. We note four outlier measurements with small error bars close to BJD epoch 2 456 500 with measured RVs around -20 m s^{-1}, whereas the other measurements taken around the same epoch show values around -12 m s^{-1}. We excluded these outlier measurements in our analyses (see Appendix B and Sect. 4.3). We used the MCMC approach applied to the HIRES data to fit a linear trend to the HARPS data. We derived an acceleration of -1.46 ± 0.02 m s^{-1} yr^{-1} (68%), which is within the uncertainties

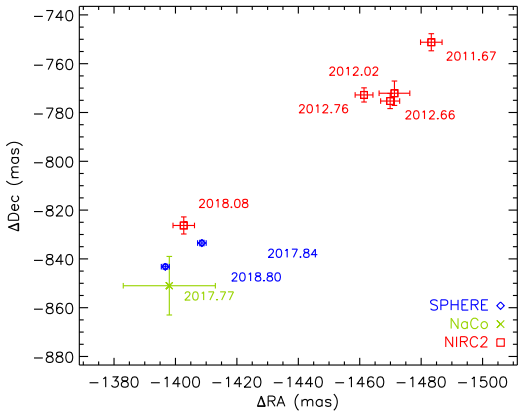

Fig. 5. Compilation of the SPHERE, Keck, and NaCo imaging measurements of the position of HD 19467B relative to the host star in the RA–Dec plane. The orbital motion in the clockwise direction between the first Keck epochs and the SPHERE and NaCo epochs can be seen (see also Fig. 6). The Keck and NaCo measurements are not recalibrated (see text).

of our HIRES acceleration estimate, and a post-upgrade offset of 12.8 ± 0.3 m s^{-1} (68%).

The systematic offset between the HIRES and HARPS measurements is related to the different zero-points of the instruments. From an MCMC linear fit to the HIRES and HARPS data, we find that the HIRES measurements are shifted by -4.0 ± 0.3 m s^{-1} (68%) compared to the HARPS data. We used this value as initial guess in the orbital fit (Sect. 4). For the orbital fit, we also added quadratically to the HIRES and HARPS measurement uncertainties jitter terms with initial guesses of 3.40 and 1.44 m s^{-1}, respectively. The values were estimated using the statistics of the dispersion of each set of measurements with respect to the predicted values from a robust linear fit. We also verified that they are close to the minimum χ^2 values using the individual RV likelihood terms (Sect. 4.3). Crepp et al. (2014) note that given the $\log R'_{\rm HK}$ and $B-V$ color of the star, the expected level of astrophysical noise due to the stellar activity should be 2.4 ± 0.4 m s^{-1}.

4. Orbital analysis

4.1. Orbital motion

The astrometry of the brown dwarf is provided in Table 3. The data are represented in the RA–Dec plane in Fig. 5 with the NIRC2 measurements reported by Crepp et al. (2014) and Bowler et al. (2020). We used a weighted average of two NIRC2 measurements obtained on 2012 January 7 by Crepp et al. (2014). The SPHERE data confirm the orbital motion of HD 19467B in the clockwise direction noted by Crepp et al. (2014), which is inconsistent with the motion expected if it were a stationary background object (HD 19467 is a high-proper motion star with $\mu_\alpha = -8.685 \pm 0.070$ mas yr^{-1}, $\mu_\delta = -260.566 \pm 0.077$ mas yr^{-1}, Gaia Collaboration 2018). Using the SPHERE data, we estimated an orbital motion of 16 ± 3 mas yr^{-1}, which is more precise but still within the uncertainties of the estimate of 22 ± 6 mas yr^{-1} in Crepp et al. (2014). Figure 6 shows the temporal evolution of the separation and position angle with time. In ~6.5 yr, the companion got closer to the star by $\sim 28 \pm 5$ mas and its position angle decreased by $\sim 3.4 \pm 0.3°$.

When comparing the trends observed for the NIRC2 data and the SPHERE data separately, we note systematic offsets. In particular, the separation measured with NIRC2 in January 2018 (1628 ± 5 mas) is shorter than the separation measured with SPHERE in November 2017 (1636.7 ± 1.8 mas, Table 3). The trends measured for the separation and the position angle from each data series separately agree (we find -5.46 ± 0.96 mas yr^{-1} and $-0.536 \pm 0.053°$ yr^{-1} using the NIRC2 data). Then, we used MCMC linear fits to the SPHERE, Keck, and NaCo data to assess potential systematics between the data series assuming the SPHERE data series as reference. The fits confirm that the separations measured with Keck are shorter by a factor of $0.9956^{+0.0030}_{-0.0031}$ at 68% and that the position angle mesured with NaCo is offset ($-0.75^{+0.48}_{-0.47}$ deg at 68%). The position angles mesured with Keck may be offset ($0.21 \pm 0.30°$ at 68%). For the Bayesian rejection fit to the imaging data only (Appendix A), we corrected the NIRC2 and NaCo position angles as well as the NIRC2 separations for the systematics measured above. In the MCMC orbital fits (Sect. 4.3 and Appendix B), we included additional free parameters to account for the systematics. Linear fits to the SPHERE data and the recalibrated NIRC2 and NaCo data give variation rates of -5.48 ± 0.44 mas/yr for the separation and of $-0.499 \pm 0.022°$ yr^{-1} for the position angle.

When fitting the NIRC2 data with linear fits robust to outliers, we find a minimum reduced χ^2 larger than 1 for the position angles. This implies that some measured uncertainties are somewhat underestimated. In particular, the position angle measured on 2011 August 30 by Crepp et al. (2014) is deviant from the fit by more than 1σ. We accordingly increased the uncertainty on this measurement for the orbital fits.

4.2. Minimum dynamical mass of HD 19467B

We used the approach in Torres (1999), Liu et al. (2002), and Bowler (2016) to assess the minimum dynamical mass of HD 19467B using our RV acceleration estimated from the HARPS data and the *Gaia* parallax. We assumed Gaussian distributions for the RV acceleration, system distance, and projected separation of the companion. We assumed for the projected separation of the companion a value of 1660 ± 7 mas using a weighted average of the measurements in Crepp et al. (2014). We derived a value of 60.0 ± 1.7 M_J (68% interval), which points toward larger masses than the $51.9^{+3.6}_{-4.3}$ M_J value in Crepp et al. (2014). The larger masses that we derived are due to the use of the *Gaia* parallax (which is smaller than the HIPPARCOS parallax) and of our measured acceleration.

4.3. Determination of the orbital parameters

We performed a simultaneous fit of the SPHERE and NIRC2 astrometry with the HIRES and HARPS RV measurements. We also included in the fit astrometric constraints from proper motion measurements of the star from HIPPARCOS and *Gaia* as done, for example, by Calissendorff & Janson (2018) and Brandt et al. (2019b) for the orbital analysis of the T-type brown dwarf GJ 758B. No clear proper motion anomaly of the HIPPARCOS and *Gaia* measurements with respect to the long-term proper motion is seen for HD 19467B in the catalog of Kervella et al. (2019): pmra_g_hg = -0.165 ± 0.088 mas yr^{-1}, pmdec_g_hg = 0.016 ± 0.094 mas yr^{-1}, pmra_h_hg = 0.640 ± 0.630 mas yr^{-1}, pmdec_h_hg = -0.170 ± 0.710 mas yr^{-1}. The HIPPARCOS reduction (van Leeuwen 2007) is well behaved with a goodness-of-fit parameter below 5. From Kervella et al. (2019), the *Gaia* DR2 record (Gaia Collaboration 2018) is well behaved with a renormalized unit weight error below 1.4 (Lindegren et al. 2018). The proper motion anomaly measurements of

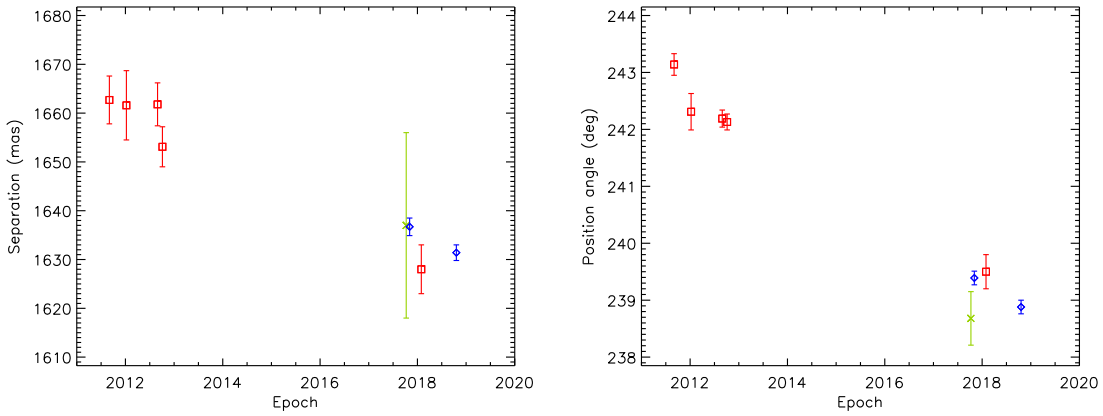

Fig. 6. Temporal evolution of the relative separation (*left*) and of the position angle (*right*) of HD 19467B measured with Keck, SPHERE, and NaCo imaging. The Keck and NaCo measurements are not recalibrated (see text).

Kervella et al. (2019) agree well within the uncertainties with the measurements in Brandt (2018, 2019) but are slighly better constrained: pmra_g_hg = -0.164 ± 0.109 mas yr^{-1}, pmdec_g_hg = 0.030 ± 0.120 mas yr^{-1}, pmra_h_hg = 0.608 ± 0.734 mas yr^{-1}, pmdec_h_hg = 0.355 ± 0.791 mas yr^{-1}.

We fit the measurements simultaneously using the Parallel-Tempered MCMC algorithm provided in the package `emcee` (Foreman-Mackey et al. 2013), which is based on the algorithm described by Earl & Deem (2005). Our implementation follows Brandt et al. (2019b) by and large (see also Maire et al. 2020). We sampled the parameter space of our 17-parameter model assuming 20 temperatures for the chains and 100 walkers. The first 8 parameters are the semi-major axis a, the eccentricity e and the argument of the periastron passage ω (parameterized as $\sqrt{e}\cos\omega$ and $\sqrt{e}\sin\omega$ to mitigate the Lucy-Sweeney bias toward low eccentricities, Lucy & Sweeney 1971), the inclination i, the longitude of the ascending node Ω, the time at the periastron passage T_0, the RV semi-amplitude of the star κ_A, and the systemic velocity γ. We present the results for Ω and ω as relative to the companion. The systemic velocity was fixed to zero because HIRES cannot measure it and we subtracted it from the HARPS data to combine both datasets.

The initial state of the sampler was set assuming uniform priors in $\log a$, $\sqrt{e}\cos\omega$, $\sqrt{e}\sin\omega$, Ω, T_0, and κ_A, as well as a $\sin i$ prior for i. The width of the priors were selected from the results of a preliminary fit to the data. First, we fit the imaging data only (Appendix A) to estimate first ranges for the period ($\log P = 5.0$–5.3, with P expressed in days), the eccentricity ($e = 0$–0.7), and the inclination ($i = 110$–$150°$). Then, we employed a least-square Monte Carlo approach (Maire et al. 2015; Schlieder et al. 2016) to fit the imaging and RV data simultaneously and derive a first range for the RV semi-amplitude (0.08–0.23 km s^{-1}). The resulting parameter distributions did not show multimodality. We present the results of an MCMC fit to the imaging and RV data in Appendix B.

The next two parameters are the parallax and semi-major axis of the orbit of the star around the center of mass of the system. For the parallax, we drew the initial guesses around the nominal value measured by *Gaia* assuming a combination of a Gaussian distribution for the measurement uncertainties and a uniform distribution for the potential systematics. We drew the semi-major axis of the star around a guess value computed from its mass (0.95 $M_\odot$), the companion mass (0.065 $M_\odot$), and the total semi-major axis, assuming a log-flat distribution with a half-width of 20 mas. The last free parameters in the model are two RV offsets, two RV jitters, one scaling factor for the NIRC2 separation, and two offsets for the NIRC2 and NaCo position angles (Sect. 4.1). We assumed uniform priors for the RV offsets with halfwidths 0.5 m s^{-1} and log-flat priors for the RV jitters with halfwidths 0.3 m s^{-1}. We assumed uniform priors for the scaling factor for the Keck separations and for the offsets for the Keck and NaCo position angles with widths 0.002, 0.05°, and 0.1°, respectively.

We ran the MCMC for 125 000 iterations and checked the convergence of the chains using the integrated autocorrelation time (Foreman-Mackey et al. 2013; Goodman & Weare 2010). The posterior distributions shown in Fig. 7 were obtained after thinning the chains by a factor 100 to mitigate the correlations and discarding the first 75% of the chains as the burn-in phase.

4.4. Parameter intervals and correlations

Figure 7 provides the histogram distributions of the parameters and the correlation diagrams. Despite the poor orbital coverage of the data and the absence of orbital curvature, most orbital parameters are relatively well constrained except for the semi-major axis, period, and time at the periastron passage. The improvements over an orbital fit of the imaging data (Appendix A) and an orbital fit of the imaging and RV data (Appendix B) are noticeable for all parameters in common. In particular, the inclusion of the RV data allows us to break the ambiguity in the longitude of the node and the argument of the periastron inherent to the fit of imaging data only. The semi-major axis of the star with respect to the center of mass of the system is poorly constrained by the current astrometric data (we forced it to stay in the range [57–177] mas). This results in loose constraints on the mass of the companion with a posterior distribution extending to masses beyond the hydrogen-burning mass limit. We derived a 68% interval of 65–86 M_J. The constraints on the semi-major axis, time at the periastron, companion mass, inclination, and RV semi-amplitude are improved compared to those derived from an RV-imaging fit. Nevertheless, this behavior is due to the constraints that we imposed on the semi-major axis of the star with respect to the center of mass of the system as seen by the correlations in Fig. 7. Chabrier & Baraffe (1997) computed hydrogen-burning mass limits of 0.072 $M_\odot$ at solar metallicity and 0.083 $M_\odot$ at [M/H] = −1. If we assume for HD 19467B the same metallicity as its host star, a linear interpolation gives a mass limit of ∼0.074 $M_\odot$ or 77 M_J. The median values with 1σ uncertainties and the best-fit values of the parameters are given in Table 5. A sample of model orbits

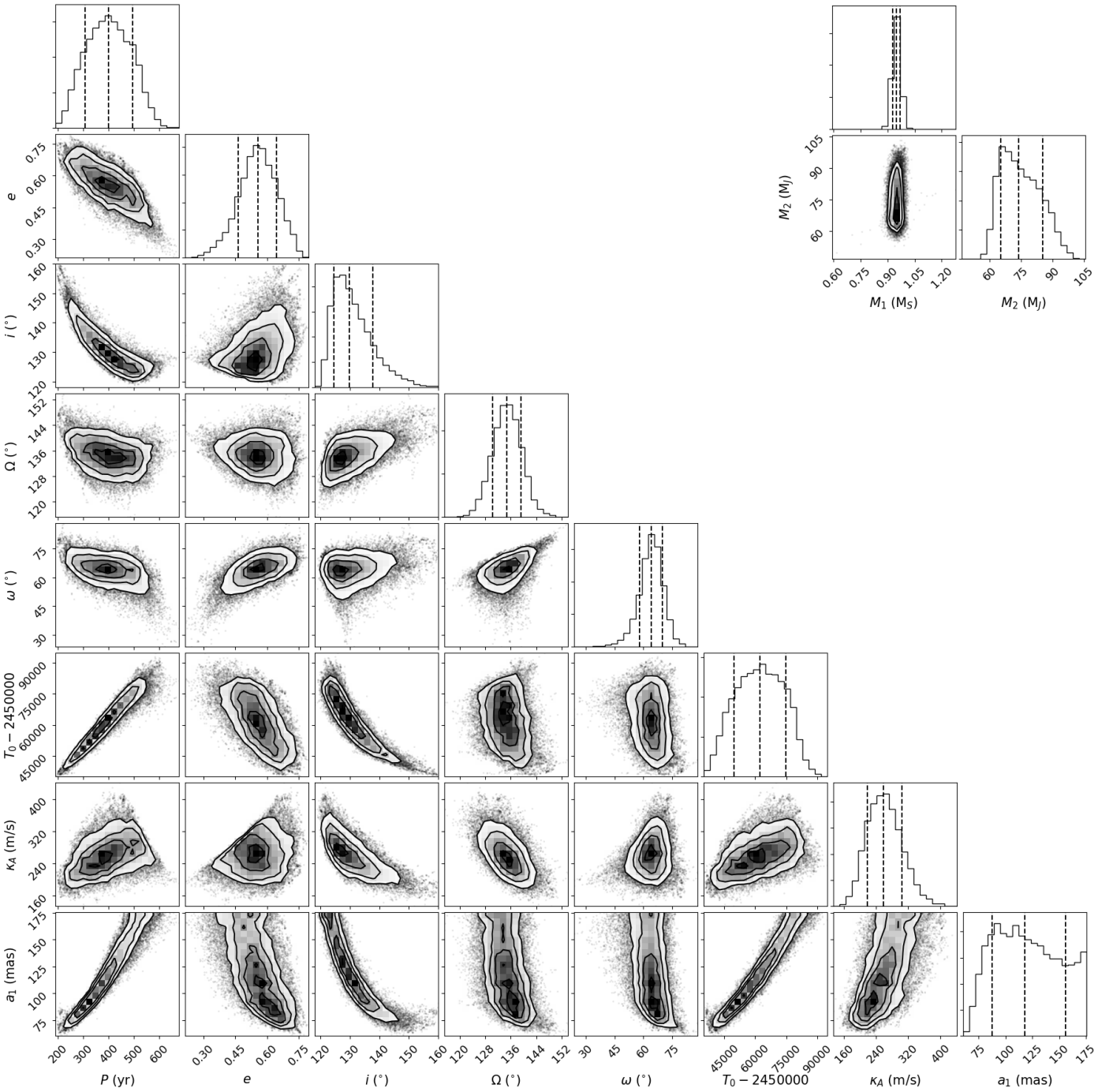

Fig. 7. MCMC samples from the posteriors of the orbital parameters (*left*) and of the masses of HD 19467 A and B (*top right*) obtained by fitting the imaging, RV, and astrometric data. The diagrams displayed on the diagonal from *top left to lower right* represent the 1D histogram distributions for the individual elements. The off-diagonal diagrams show the correlations between pairs of orbital elements. In the histograms, the dashed vertical lines indicate the 16, 50, and 84% quantiles.

are represented in Fig. 8. For the comparison of the companion properties to model predictions (Sect. 6), we consider a mass range for the companion of 65–77 M_J.

5. Spectral analysis

5.1. Comparison to color-magnitude diagrams

We used the IRDIS dual-band photometry of the companion to compute the color-magnitude diagrams shown in the top panels of Fig. 9 (see details in Appendix C, and Appendix C of Bonnefoy et al. 2018). We also used the broad-band photometry of HD 19467B in Crepp et al. (2014) (we recomputed the absolute magnitudes to account for the new distance estimate from the *Gaia* parallax) and in our analysis to compute the color-magnitude diagrams shown in the bottom panels of Fig. 9. For these last diagrams, we show for comparison the evolutionary tracks for an age of 8 Gyr from the COND model (Baraffe et al. 2003) and the DUSTY model (Chabrier et al. 2000). In all panels, we indicate for comparison the T-type substellar companions 51 Eridani b (Macintosh et al. 2015; Samland et al. 2017; Rajan et al. 2017), GJ 758B (Thalmann et al. 2009; Janson et al. 2011;

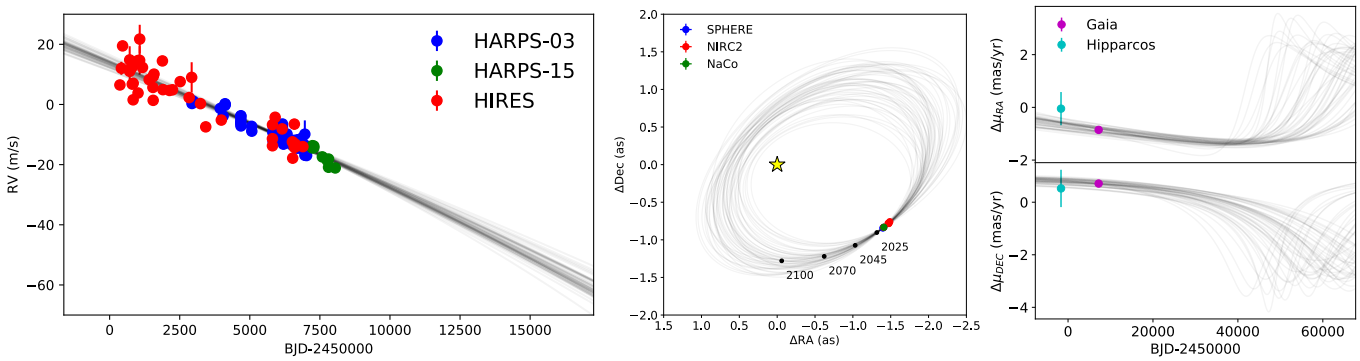

Fig. 8. Sample of 50 model orbits (gray curves) fitted on the HD 19467B data (colored points) from RV (*left*), imaging (*middle*), and astrometry (*right*). In the *middle* panel, the yellow star marks the location of the star and the black dots show the median predicted position for a few epochs in the future.

Table 5. Orbital parameters and dynamical mass of HD 19467B.

Parameter	Unit	Median ± 1σ	Best fit
Fitted parameters			
Semi-major axis a	mas	1699^{+269}_{-277}	1416
$\sqrt{e}\cos\omega$		-0.32 ± 0.06	−0.34
$\sqrt{e}\sin\omega$		$-0.67^{+0.09}_{-0.07}$	−0.72
Inclination i	°	$129.8^{+8.1}_{-5.1}$	137.2
PA of asc. node Ω	°	134.8 ± 4.5	134.1
Time periastron T_0	BJD	$2\,512\,264^{+12428}_{-12\,637}$	2 498 964
RV semi-ampl. κ_A	m s^{-1}	259^{+46}_{-41}	245
Parallax π	mas	31.22 ± 0.12	31.25
SMA primary a_1	mas	118^{+38}_{-30}	89
RV offset ZP_{HARPS}	m s^{-1}	12.8 ± 0.7	13.1
RV offset ZP_{HIRES}	m s^{-1}	-4.0 ± 0.9	−3.7
RV jitter σ_{HARPS}	m s^{-1}	$1.49^{+0.18}_{-0.15}$	1.39
RV jitter σ_{HIRES}	m s^{-1}	$3.9^{+0.6}_{-0.5}$	3.9
Sep. scaling $f\rho_{NIRC2}$		$0.9955^{+0.0034}_{-0.0032}$	0.9947
PA offset ΔPA_{NIRC2}	°	0.16 ± 0.31	0.31
PA offset ΔPA_{NaCo}	°	-0.74 ± 0.53	−1.23
Computed parameters			
M_1	$M_\odot$	0.95 ± 0.02	0.94
M_2	M_J	74^{+12}_{-9}	66
Mass ratio M_2/M_1		$0.074^{+0.012}_{-0.009}$	0.067
Period P	yr	398^{+95}_{-93}	304
Semi-major axis a	au	54 ± 9	45
Eccentricity e		0.56 ± 0.09	0.64
Arg. periastron ω	°	$64.2^{+5.5}_{-6.3}$	64.5

Vigan et al. 2016), GJ 504B (Kuzuhara et al. 2013; Janson et al. 2013; Bonnefoy et al. 2018), and the binary brown dwarf ϵ Ind BC (King et al. 2010). For the bottom-left panel only, we indicate SCR 1845-6357B (Biller et al. 2006; Kasper et al. 2007). We accounted for the new distance estimates from *Gaia* when computing the absolute magnitudes of the companions, except for ϵ Ind BC for which we used the HIPPARCOS parallax (van Leeuwen 2007).

HD 19467B is located near mid-T template dwarfs in the IRDIS color-magnitude diagrams, which supports its spectral type of T5.5 ± 1.0 derived in Crepp et al. (2015). It follows the predictions from the COND model for a mass of ∼65 M_J in the color-magnitude diagrams computed from the broad-band photometry. This suggests that atmospheric models with no or very thin clouds should reproduce the spectral properties of HD 19467B well. The companion is brighter in absolute magnitude than 51 Eridani b, GJ 758B, and GJ 504B and shows bluer colors in the broad-band color-magnitude diagrams. This could be explained by its larger mass, earlier spectral type, and/or older age. Finally, the companion lies close to SCR 1845-6357B, which suggests that they share similar spectral properties. SCR 1845-6357B has a spectral type of T6, $T_{\rm eff} = 950$ K, $\log g = 5.1$ dex, and a mass of 40–50 M_J assuming a system age of 1.8–3.1 Gyr (Biller et al. 2006; Kasper et al. 2007). HD 19467B is also close to ϵ Ind C, which has a spectral type of T6, $T_{\rm eff} = 880$–940 K, $\log g = 5.25$ dex, and a dynamical mass of 70.1 ± 0.7 M_J (King et al. 2010; Dieterich et al. 2018). Kasper et al. (2009) find for ϵ Ind C $T_{\rm eff} = 875$–925 K and $\log g = 4.9$–5.1 dex.

5.2. Atmospheric model fitting

We converted the contrast measurements of HD 19467B reported in Crepp et al. (2014) and in Table 4 into physical fluxes using a model stellar spectrum ($T_{\rm eff} = 5700$ K, $\log g = 4.5$ dex, and [Fe/H] = 0.0 dex) from the BT-NextGen library (Allard et al. 2012) and the filter transmission curves. We fit the model spectrum to the stellar spectral energy distribution (SED) over the range 0.3–12 μm using the chi-square fitting tool provided in the Virtual Observatory SED Analyzer (Bayo et al. 2008). We assumed that the visual extinction is zero given the vicinity of the star to the Sun. The SED was built using data from *Tycho* (Høg et al. 2000), 2MASS (Cutri et al. 2003), WISE (Cutri & et al. 2013), and IRAS (Helou & Walker 1988), as well as Johnson photometry (Mermilliod 2006) and Strömgren photometry (Paunzen 2015). We also extracted the normalized P1640 spectrum presented in Crepp et al. (2015) using `WebPlotDigitizer` (Rohatgi 2019) and converted it to physical fluxes using as reference the NIRC2 photometry measured in the J band.

5.2.1. Exo-REM models

As the first approach to characterize the atmosphere of HD 19467B, we fit the SED with the spectral library Exo-REM (Baudino et al. 2015, 2017; Charnay et al. 2018, see Table 6).

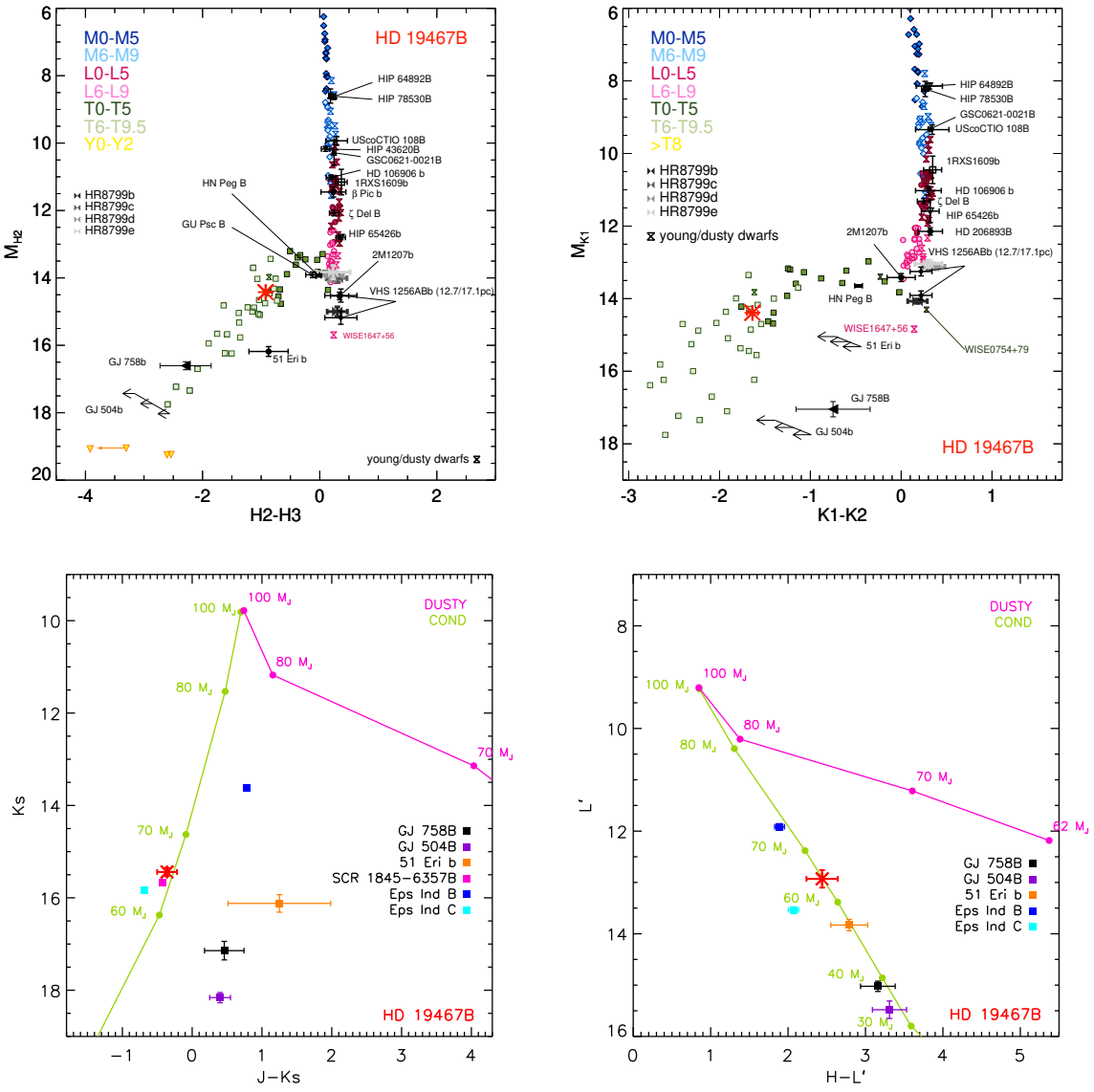

Fig. 9. *Top*: color-magnitude diagrams of HD 19467B (red star) using the SPHERE narrow-band photometry. Template dwarfs (colored points) and a few young low-mass companions (indicated by black labels) are also shown for comparison. *Bottom*: color-magnitude diagrams of HD 19467B using the Keck and NaCo broad-band photometry. Evolutionary tracks from the COND model (Baraffe et al. 2003) and DUSTY model (Chabrier et al. 2000) for an age of 8 Gyr are also indicated with a few known T-type low-mass companions (colored points).

Table 6. Characteristics of the atmospheric model grids adjusted on the SED of HD 19467B (see text).

Model name	$T_{\rm eff}$ (K)	$\Delta T_{\rm eff}$ (K)	$\log(g)$ (dex)	$\Delta\log(g)$ (dex)	[Fe/H] (dex)	Δ[Fe/H] (dex)	Clouds	$f_{\rm sed}$ or $f_{\rm sat}$	$\Delta f_{\rm sed}$ or $\Delta f_{\rm sat}$
petitCODE-cloud free	500–1700	50	3.0–6.0	0.5	−1.0–1.4	0.2	No	–	–
petitCODE-cloudy	800–1300	50	1.5–6.0	0.5	−0.4–1.4	0.2	Yes	0.5–6.0	0.5
Exo-REM	500–2000	50	3.0–6.0	0.1	−0.5–0.5	0.5	No, Yes	0.1, 0.01	–
Morley 2012	400–1300	50/100	4.0–5.5	0.5	0.0	–	Yes	2.0–5.0	1.0

Notes. The columns give the model name, the range and step for the effective temperature, surface gravity, and metallicity, the type of clouds included in the model, and the range and step for the sedimentation or the saturation parameter for the clouds (see text).

The analysis was similar to the one introduced in Baudino et al. (2015), using χ^2 maps. We explored the $T_{\rm eff}$ (between 500 and 2000 K by step of 50 K) and $\log g$ (between 3 and 6 by step of 0.1) for six cases: metallicity [Fe/H] = −0.5, 0, +0.5, without clouds or with simple microphysics clouds (described in Charnay et al. 2018). The species assumed for the clouds were iron (Fe) and silicates (Mg_2SiO_4). We included in the analysis a complete research of the optimal radius. Usually, we approximate the radius as a shift of the full spectrum (Baudino et al. 2015). For this analysis, we first performed a simple χ^2 minimization as usual. If the radius was outside a given range (0.7–1.3 R_J in this case, coming from evolutionary tracks), we tried to force

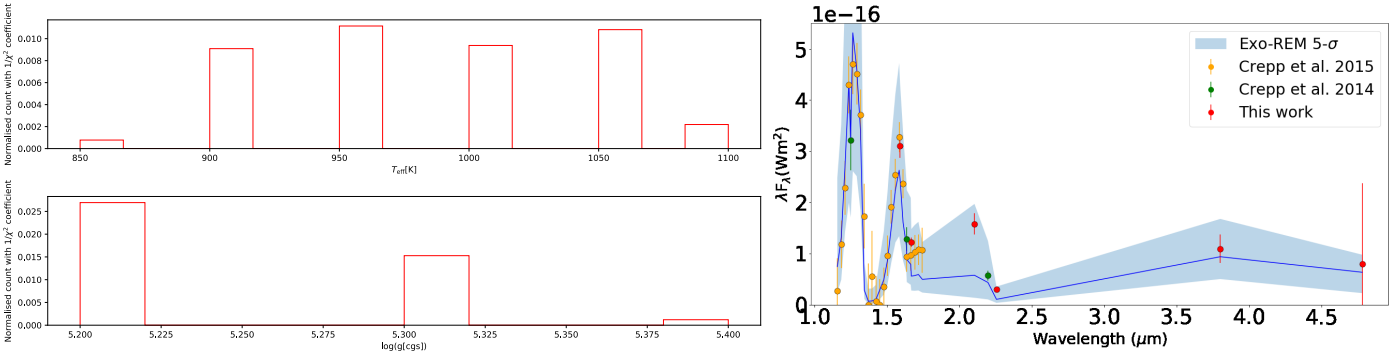

Fig. 10. *Left*: histograms of the effective temperature (*top*) and surface gravity (*bottom*) of the models from Exo-REM, reproducing the data, without cloud covering all metallicity values (see text). The number of count is normalized using the invert of the χ^2. *Right*: comparison of the best-fit model spectra (dark blue line: best fit, light blue area: 5σ envelope) and of the mesured SED (colored data points).

Table 7. Retrieved HD 19467B's atmospheric parameters.

Model name	$T_{\rm eff-cloudy}$ (K)	$T_{\rm eff-cloud-free}$ (K)	$\log g$ (dex)	[Fe/H] (dex)	$f_{\rm sed}$	CF	R_p (R_J)	M_p (M_J)	$\chi^2_{\rm min}$
Exo-REM-cloud free	–	975 ± 125	5.2 ± 0.1	UC	–	(1.0)	–	–	231
petitCODE-cloud free	–	1186^{+24}_{-27}	$5.61^{+0.06}_{-0.05}$	$0.18^{+0.12}_{-0.11}$	–	(0.0)	$0.59^{+0.03}_{-0.03}$	57^{+7}_{-4}	103.3
petitCODE-cloudy	1044^{+12}_{-18}	–	$5.33^{+0.05}_{-0.05}$	$-0.05^{+0.07}_{-0.07}$	$1.02^{+0.39}_{-0.28}$	(1.0)	$0.84^{+0.04}_{-0.02}$	63^{+6}_{-7}	101.3
petitCODE-patchy	932^{+66}_{-63}	1291^{+99}_{-89}	$5.34^{+0.08}_{-0.09}$	$0.03^{+0.08}_{-0.08}$	$1.20^{+0.79}_{-0.46}$	$0.79^{+0.10}_{-0.15}$	$0.83^{+0.09}_{-0.06}$	60^{+7}_{-6}	86.6
Morley 2012	928^{+39}_{-42}	–	$5.20^{+0.09}_{-0.10}$	(0.0)	$4.07^{+0.41}_{-0.49}$	(1.0)	$0.99^{+0.10}_{-0.09}$	63^{+6}_{-7}	129.7

Notes. Values given in parenthesis are priors or assumptions and are not retrieved (see text). UC: unconstrained.

the radius to decrease or increase to fit in this range. The only rule was to stay in the confidence interval (5σ).

In these χ^2 maps, we only kept the results that reproduced the data at less than 5-σ, with a radius solution between 0.7–1.3 R_J and a mass solution between 52–72 M_J (based on the system's dynamics). Although the adopted mass prior includes smaller values than the actual constraints from the orbital fit (Sect. 4.3), the choice of the bounds has a negligible effect on the derivation of the atmospheric parameters. The radius prior has a larger effect. The models fit the data only without clouds (the best fit with clouds is out at more than 10σ). We do not observe any clues about the metallicity. Figure 10 shows the histograms of the $T_{\rm eff}$ and $\log g$ reproducing the data and the comparison of the best-fit spectra to the measured SED. The count of the histograms is normalized using the invert of the χ^2 as a coefficient to highlight the best-fit cases. The inferred $T_{\rm eff}$ is 975 ± 125 K, the inferred $\log(g[\rm cgs]) = 5.2 \pm 0.1$ (Table 7). We also provide in Table 7 the χ^2 values associated with the best-fit solution computed according to the definition of Baudino et al. (2015).

5.2.2. petitCODE models

As the second approach, we used petitCODE (Mollière et al. 2015, 2017) to calculate a grid of self-consistent models; assuming both cloud-free and cloudy atmospheres. The characteristics of these models are summarized in Table 6. For the cloudy models, the species included are Na_2S and KCl. The free parameters in the cloud-free models are the effective temperature, the surface gravity, and the metallicity. For the cloudy models, the sedimentation factor ($f_{\rm sed}$) is also taken into account as a free parameter.

We performed Bayesian analysis using the `emcee` tool (Foreman-Mackey et al. 2013) to explore the atmospheric properties of HD 19467B with the petitCODE models. We considered the statistical treatment of observational uncertainties and explored any underestimation of these uncertainties through a Gaussian Process. Uninformative priors were also assumed for the initialization of the walkers in the MCMC process.

Firstly, we fit the data with cloud-free models. Figure 11 shows the results and the corner plot of the retrieved parameters. The retrieved properties of HD 19467B are as follows, assuming a cloud-free atmosphere (Table 7): an effective temperature of 1186^{+24}_{-27} K, a surface gravity of $5.61^{+0.06}_{-0.05}$ dex, and a metallicity of $0.18^{+0.12}_{-0.11}$ dex. The radius is $0.59^{+0.03}_{-0.03}$ R_J and the mass is 57^{+7}_{-4} M_J. As discussed, cloud-free models could explain the SED, although tentatively. The photometric points, in particular at 1.633 μm, 2.255 μm, and 3.8 μm, disagree with the best-fit model, with the first two by at least 3σ (dotted lines in the bottom panel of Fig. 11). In addition, the inferred radius of the companion is significantly smaller than the expected radius from the evolutionary tracks (0.8 R_J). We therefore examined cloudy models to improve the fit.

Secondly, we fit the data with cloudy models. We assumed $52 < M_p < 72$ M_J and $0.7 < R_p < 1.3$ R_J as priors. Figure 12 shows the fitted models to the data and the corner plot of the retrieved parameters. The retrieved atmospheric properties are as follows (Table 7): $T_{\rm eff} = 1044^{+12}_{-18}$ K, $\log g = 5.33^{+0.05}_{-0.05}$ dex, and $[\rm Fe/H] = -0.05^{+0.07}_{-0.07}$ dex, all have values less than their counterparts when fitting with petitCODE cloud-free models. This behavior can be explained by the prior used for the companion radius, which excludes radii smaller than 0.7 R_J. The best-fit value for $\log(f_{\rm sed})$ is $0.01^{+0.14}_{-0.14}$, which corresponds to a